



Atom-specific forces and defect identification on surface-oxidized Cu(100) with combined 3D-AFM and STM measurements

Mehmet Z. Baykara,^{1,2,3,*} Milica Todorović,^{4,*} Harry Mönig,^{1,2,5} Todd C. Schwendemann,^{1,2,6} Özhan Ünverdi,^{1,2} Lucia Rodrigo,⁴ Eric I. Altman,^{2,7} Rubén Pérez,^{4,†} and Udo D. Schwarz^{1,2,7,‡}

¹*Department of Mechanical Engineering and Materials Science, Yale University, New Haven, Connecticut 06520, USA*

²*Center for Research on Interface Structures and Phenomena (CRISP), Yale University, New Haven, Connecticut 06520, USA*

³*Department of Mechanical Engineering and UNAM-Institute of Materials Science and Nanotechnology, Bilkent University, 06800 Bilkent, Ankara, Turkey*

⁴*Departamento de Física Teórica de la Materia Condensada and Condensed Matter Physics Center, Universidad Autónoma de Madrid, 28049 Madrid, Spain*

⁵*Institute of Physics and Center for Nanotechnology (CeNTech), University of Münster, 48149 Münster, Germany*

⁶*Department of Physics, Southern Connecticut State University, New Haven, Connecticut 06515, USA*

⁷*Department of Chemical and Environmental Engineering, Yale University, New Haven, Connecticut 06520, USA*

(Received 31 January 2013; published 12 April 2013)

The influence of defects on the local structural, electronic, and chemical properties of a surface oxide on Cu(100) were investigated using atomic resolution three-dimensional force mapping combined with tunneling current measurements and *ab initio* density functional theory. Results reveal that the maximum attractive force between tip and sample occurs above the oxygen atoms; theory indicates that the tip, in this case, terminates in a Cu atom. Meanwhile, simultaneously acquired tunneling current images emphasize the positions of Cu atoms, thereby, providing species-selective contrast in the two complementary data channels. One immediate outcome is that defects due to the displacement of surface copper are exposed in the current maps, even though force maps only reflect a well-ordered oxygen sublattice. The exact nature of the defects is confirmed by the simulations, which also reveal that the arrangement of the oxygen atoms is not disrupted by the copper displacement. In addition, the experimental force maps uncover a position-dependent modulation of the attractive forces between the surface oxygen and the copper-terminated tips, which is found to reflect the surface's inhomogeneous chemical and structural environment. As a consequence, the demonstrated method has the potential to directly probe how defects affect surface chemical interactions.

DOI: [10.1103/PhysRevB.87.155414](https://doi.org/10.1103/PhysRevB.87.155414)

PACS number(s): 31.15.A–, 68.37.Ps, 68.35.Dv, 68.47.Gh

I. INTRODUCTION

When an atom or molecule approaching a surface ultimately makes contact, what happens next depends critically on its ability to interact with that surface. To be able to influence the events following the atom's/molecule's arrival towards a desired outcome, a detailed, atomic-scale knowledge of the specifics of the atom/molecule-surface interaction is needed. This knowledge is particularly important to understand mechanical phenomena, such as adhesion or friction, physical processes, such as those governing thin-film growth as well as chemical reactions occurring during surface oxidation, corrosion, or heterogeneous catalysis.^{1,2} Despite the considerable success of scanning tunneling microscopy (STM) in providing atomic-scale information about surface phenomena^{3,4} (e.g., the determination of preferred adsorption sites⁵ and activation barriers for diffusion,⁶ characterizing adsorbate-adsorbate interactions⁷ as well as observing surface reconstructions⁸ and reactions on the atomic scale),⁹ it does not deliver quantitative information regarding local chemical interaction forces associated with specific atomic sites on the sample surface through these approaches.

Noncontact atomic force microscopy (NC-AFM), on the other hand, can be utilized to perform atomic-resolution force spectroscopy, leading to a quantitative characterization of the force interactions between specific atomic sites on a surface of interest and a local probe (the microscope's tip).^{10–12} Impressive accomplishments obtained with NC-AFM

in recent years include the chemical identification of single atoms,¹³ high-resolution imaging and identification of individual organic molecules,¹⁴ localization and discrimination of individual chemical bonds,^{15,16} as well as mapping the charge distribution within a single molecule.¹⁷ Moreover, the extension of local force measurements to all three spatial dimensions has led to the establishment of the three-dimensional atomic force microscopy (3D-AFM) technique, which enables the recording of full quantitative three-dimensional maps of interaction forces on surfaces with atomic resolution.^{18–20} The additional recording of the tunneling current during NC-AFM experiments has allowed the simultaneous characterization of electronic properties associated with surface atoms, resulting in the acquisition of complementary physical information from multiple data channels.^{21–23}

Metal oxides, which are of great importance for a number of fields, such as microelectronics and catalysis,²⁴ have frequently been investigated by NC-AFM imaging and force spectroscopy experiments in the past.^{12,25,26} Based on this general scientific and technological interest and the fact that they feature multiple chemical species that can be accessed individually by a local probe, metal oxides are well suited for 3D-AFM investigations where variations in interaction forces on metal and oxygen atoms ought to be quantified and compared. In addition, chemical imaging/identification can be aided by simultaneous STM measurements where images tend to reflect the more conductive metallic surface species. Finally,

since metal-oxide surfaces frequently feature atomic-scale surface defects, such combined 3D-AFM/STM experiments present a good opportunity to investigate defect structures and their effects on tip-sample interactions.

Motivated by the issues outlined above, we conducted a 3D-AFM study of the Cu(100)-O surface [*in situ* surface oxidized Cu(100)], combined with simultaneous tunneling current measurements and *ab initio* density functional theory (DFT) calculations. Force interactions associated with individual oxygen atoms on the sample surface are quantified, and the tip structure/chemistry as well as the structure of a specific surface defect associated with dislocated copper atoms are determined. It will be shown that the combination of these experimental and theoretical methods allows the assignment of force and tunneling current maxima to specific oxygen and copper atoms, respectively, and the identification of dislocations in the Cu surface lattice that lead to a modulation in the attractive interactions of the oxygen atoms with the tip.

II. EXPERIMENTAL METHODS

A. Sample system

As many other transition metals, Cu-based materials are active catalysts for a number of important reactions involving oxygen including methanol synthesis,²⁷ the water-gas-shift reaction,²⁸ and the reduction of nitrogen oxides.²⁹ Additionally, understanding the behavior of surface oxides is crucial to unravel the atomic-scale details of bulk oxidation and the corrosion of metals,^{30–33} which, as a particularly well-known example, over time, bestows bulk copper its green patina. For these reasons, the oxygen-induced $(2\sqrt{2} \times \sqrt{2}) R45^\circ$ missing-row reconstruction of copper described below [referred to as Cu(100)-O] represents an attractive model system for atomic-scale investigation by 3D-AFM that is complementary to the oxidized Cu(110) surface, which had previously been investigated.³⁴

A schematic of the $(2\sqrt{2} \times \sqrt{2}) R45^\circ$ missing-row reconstructed surface is pictured in Fig. 1. In this one-monolayer-

thick reconstruction, oxygen atoms are located nearly coplanar with the copper atoms.^{35,36} Thereby, the two chemical species feature strikingly different structural arrangements: One-third of the copper atoms (Cu1) are located in the centers of the *filled* rows on the surface, whereas, the remaining Cu atoms (Cu2) are on the edges of filled rows. In contrast, oxygen (O) atoms are arranged in rectangles of equal height parallel to the missing rows (3.6 Å) but alternating width (3.5 and 3.7 Å, respectively) perpendicular to them due to a lateral relaxation towards the missing rows.³⁷

The sample preparation composed, first, the cleaning of a commercially available Cu(100) single crystal through several sputtering and annealing cycles. After confirming the surface order and cleanliness through low-energy electron diffraction (LEED) and STM measurements, the $(2\sqrt{2} \times \sqrt{2}) R45^\circ$ missing-row reconstruction was obtained by exposing the surface to 1000–3000 L of molecular oxygen at a temperature of ≈ 575 K in the same ultrahigh vacuum chamber where the sputter/anneal cycles were performed. A clear indication of the successful formation of the $(2\sqrt{2} \times \sqrt{2}) R45^\circ$ reconstruction is the observation of a very ordered surface structure by STM that is characterized by step pinning along the $\langle 001 \rangle$ directions and perpendicular domains on terraces.^{35,38–40}

B. Data acquisition

For the measurements described in this paper, we have used a homebuilt low-temperature ultrahigh vacuum NC-AFM/STM with high stability and low drift.⁴¹ The sample was probed with an electrochemically etched and field ion-beam-treated Pt/Ir tip, which was attached to a tuning fork in the qPlus configuration (spring constant $k \approx 2000$ N/m and resonance frequency $f_0 = 29\,177$ Hz).⁴² All measurements were performed at a temperature of 5 K with an oscillation amplitude of ≈ 1.0 nm. The three-dimensional data set of forces and tunneling currents presented in Sec. IV was acquired over ≈ 10 h using the same data acquisition and analysis schemes reported earlier in Refs. 19, 43, and 44 which were further enhanced by the simultaneous recording of tunneling currents. After drift correction (≈ 4.5 Å in both x and y directions over the course of data acquisition), the full data set was composed of 221×221 pixels laterally. The contact potential difference was roughly compensated by applying a bias voltage of $U = -0.4$ V to the sample surface. This led to very small tunneling currents with the maximum current averaged over an oscillation cycle being ≈ 6 pA at the plane of closest approach.

III. THEORETICAL CALCULATIONS

A. Defining the structural model for the Cu(100)-O surface

The first step in our theoretical approach involved DFT simulations designed to yield a precise structural model of the Cu(100)-O surface that could be used as input for the subsequent simulations of the NC-AFM and STM experiments, respectively. Towards this end, the surface was modeled using the Vienna *ab initio* simulation package (VASP) code⁴⁵ and projector augmented-wave (PAW) method^{46,47} coupled with the Perdew-Burke-Ernzerhof (PBE) exchange-correlation functional.⁴⁸ A four-layer slab model of the Cu(100)-O $(2\sqrt{2} \times \sqrt{2}) R45^\circ$ surface was constructed based on the

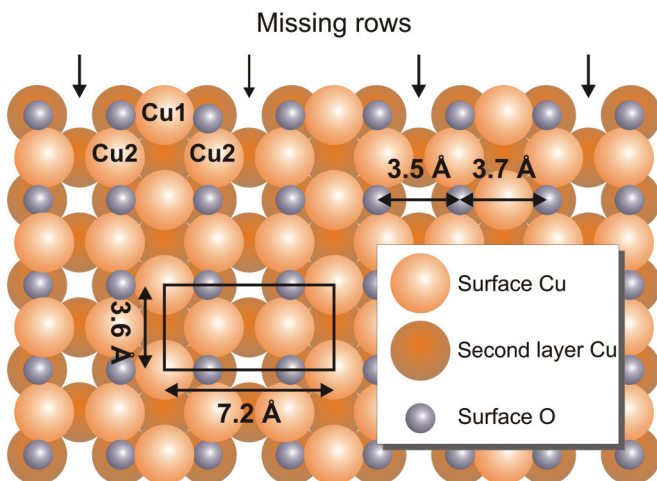


FIG. 1. (Color online) Missing-row model of the surface oxide layer on the Cu(100) surface. A rectangular unit cell, the positions of Cu1 and Cu2 atoms and the missing rows, as well as the alternating separation of O atoms are highlighted.

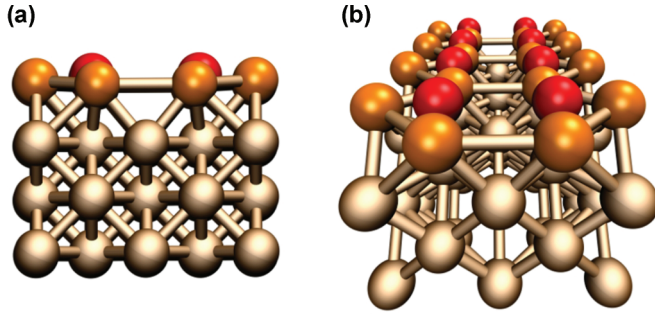


FIG. 2. (Color online) The 2×4 unit-cell segment of the optimized Cu(100)-O surface oxide structure with Cu atoms shown in gold, O atoms shown in red, and subsurface Cu slabs shown in dimmed gray. (a) The vertical displacement of surface atoms around the missing-row feature seen in the x - z plane (side view). (b) The difference in O and Cu2 atom lateral displacements towards the missing row, perspective view.

computed bulk Cu lattice constant of 3.638 \AA (bulk modulus: 138 GPa). Subsequent structural optimizations of the top two layers were performed in a 2×1 unit cell ($7.2 \times 3.6 \text{ \AA}$) with periodic boundary conditions, using a 450-eV plane-wave cutoff and a $4 \times 8 \times 1$ Monkhorst-Pack mesh for k -point sampling, until forces were smaller than 0.01 eV/\AA . The obtained missing row surface reconstruction, illustrated in Fig. 2, was in good agreement with experimental data and previous theoretical studies^{37,49} as shown in Table I: The Cu2 and O atoms both move towards the missing row (by 0.23 and 0.04 \AA , respectively). Cu1 atoms are positioned 0.13 \AA above the Cu2 atoms in the top surface layer, whereas, O atoms cap the surface at a height of 0.2 \AA above the Cu1 atoms.

For the purposes of STM image simulation, the surface was also computed using the OPENMX 3.5 DFT code⁵¹ with a basis set of optimized single- ζ pseudoatomic orbitals (PAOs) generated for a PBE exchange-correlation functional and a norm-conserving pseudopotential.⁵² Calculations of the Cu(100)-O surface (computed bulk Cu lattice parameter was 3.679 \AA) were performed in a 2×1 ($7.4 \times 3.7 \text{ \AA}$) unit cell with a PAO cutoff of 6.0 a.u. (for both Cu and O), energy cutoff of 200 Ry, $8 \times 16 \times 1$ k -point mesh, and a force tolerance of 0.01 eV/\AA . The resulting Cu(100)-O surface reconstruction and band structure were found to be in very good agreement with our VASP calculations and previously obtained data (see Table I).

B. Tip-sample force simulations

DFT simulations of tip-surface interactions responsible for the contrast observed in experimental AFM images were

performed using the VASP code⁴⁵ with a 4×4 Cu(100)-O unit cell ($14.5 \times 14.5 \text{ \AA}$), using a 420-eV plane-wave cutoff and a minimal $2 \times 2 \times 1$ Monkhorst-Pack mesh. Four different model tips (the exact structures of which are discussed in Sec. IV of this paper) were placed above six unequal sites of the Cu(100)-O surface with the tip apex initially at $d = 5 \text{ \AA}$ above the surface. Note that, in this context, d refers to the tip-sample distance controlled by the piezo displacement rather than the actual distance between the closest tip and the surface atoms, which varies due to the relaxations induced by the tip-sample interaction. The rigid parts of the tips were then lowered in steps of $\Delta d = 0.25 \text{ \AA}$; at each step, the bottom two layers of the tip and the top two layers of the Cu(100)-O surface were allowed to relax into the most energetically favorable configuration to allow for structural rearrangements. Site-dependent energies and forces of tip-surface interactions were then extracted for all four tip models used.

C. Surface defect simulations

Geometries for adatom defects (referred to as filled-row or “type-I” defects, cf. Sec. IV) were initially obtained through VASP structural optimization calculations in 4×4 Cu(100)-O unit cells, using a $4 \times 4 \times 1$ k -point mesh and a force tolerance of 0.03 eV/\AA . Simulated STM images were computed after geometry reoptimization in a larger 4×6 Cu(100)-O unit cell system with a $4 \times 3 \times 1$ k -point mesh using the OPENMX code. The alternative defect structure (displacement or “type-II” defect) was generated by a 90° rotation of two Cu2 atom pairs in a 4×6 Cu(100)-O unit cell, followed by a structural optimization ($4 \times 3 \times 1$ k -point mesh) using the OPENMX code. All defect structures were ultimately computed in larger unit cells in an attempt to eliminate any structural strain associated with periodic boundary conditions.

D. Tunneling current simulations

The nonequilibrium Green’s function (NEGF) method⁵³ was employed for the calculations of distance-dependent x - y tunneling current maps using the OPENMX electronic structure data as a representation of the sample. To generate the electronic structure of the probe, model tips identical to those used in the AFM study were grafted onto slabs of Cu(111) to generate the bulklike electronic states needed for current evaluation. The tips were placed at a height h above the surface (distance between the center of the tip apex atom and the atom defining the highest surface point) and were shifted laterally on a fine mesh as currents were computed by integration in bins of

TABLE I. Vertical and lateral displacements of Cu(100)-O surface atoms in angstroms, enabling comparison of this work to previous theoretical and experimental data. The lateral displacements were defined in reference to ideal lattice coordinates of atoms.

d (\AA)	VASP	OPENMX	DFT ³⁷	DFT ⁴⁹	Expt. ⁵⁰	Expt. ³⁶
Δz [O-lay2]	2.23	2.18	2.21	2.21	2.14	2.05
Δz [O-Cu1]	0.20	0.18	0.13	0.17	0.20	0.09
Δz [O-Cu2]	0.33	0.27	0.31	0.28	0.10	0.17
Δx [O]	0.04	0.04	0.05	0.05	0.00	0.04
Δx [Cu2]	0.23	0.33	0.19	0.25	0.30	0.29

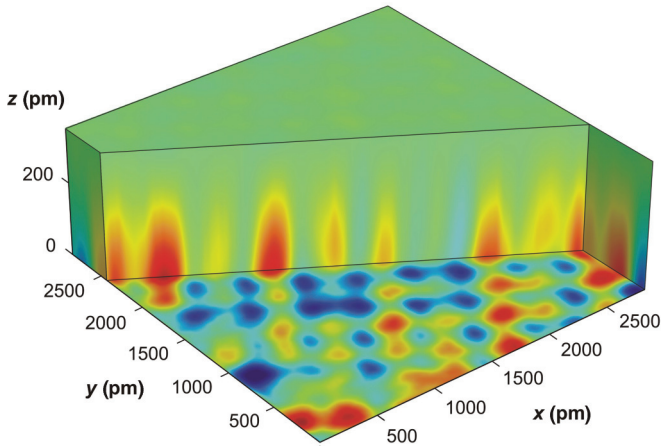


FIG. 3. (Color online) Three-dimensional representation of chemical interaction forces over an area of 2.89×2.89 nm. The color scale ranges from -12 pN (dark blue, least attractive) to $+10$ pN (dark red, most attractive) with the average force at each height subtracted.^{18,19} Note that the z axis has been arbitrarily set to $z = 0$ pm at the distance of closest approach, i.e., the displayed values do not coincide with the definition of the distance d in the simulations.

0.05 V across a bias voltage of $U = -0.4$ V that was used in experiments.

IV. RESULTS AND DISCUSSION

In order to characterize the interaction forces associated with individual atoms of the Cu(100)-O surface, 3D-AFM experiments with a simultaneous recording of tunneling current were performed. The resulting three-dimensional map of interaction forces is shown in Fig. 3. We start our discussion with the analysis of the force map of Fig. 4(a) which has been extracted from the lowest plane of the 3D data set. It should be noted that this image represents a quantitative map of the chemical interaction forces associated with the sample surface on an atomic scale at a fixed height rather than a

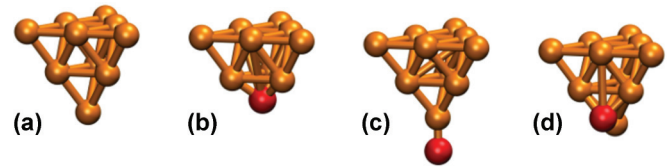


FIG. 5. (Color online) Probe tips considered in the calculations (perspective views with copper atoms in gold and oxygen atoms in red). (a) Cu-terminated tip; (b) O-terminated tip; (c) dangling bond O tip; (d) O-adatom tip (“CuO tip”).

fixed *frequency shift* map as delivered by standard NC-AFM measurements. The circular maxima observed in the image are found to have alternating separations of 3.5 and 3.7 Å in one direction, whereas, they are evenly spaced in the other direction with a periodicity of 3.6 Å. Since the only type of lattice site on the surface that features such an arrangement is oxygen atoms, one can clearly identify the maxima observed in the force channel as such; the alternating periodicity further enables the unambiguous assignment of the locations and directions of the missing rows.

This information can now be used to establish the chemical nature of the probe tip’s apex atoms. It is well documented that the contrast observed in NC-AFM measurements is strongly influenced by the structure and chemical composition of the tip apex.^{54–56} Despite recent advances, the experimental determination of the tip apex structure and chemistry remains difficult,¹⁶ which is why *ab initio* DFT calculations have been employed to identify tip apices used in specific experiments.^{54,56} As described in Sec. III, we have performed DFT calculations using a number of possible candidates, looking for tip apices that would interact most strongly with oxygen atoms of the surface. Due to the fact that the tip apex has been treated by controlled contact with the sample surface prior to data acquisition, tips with Cu and Cu-O apices have been given priority (see Fig. 5). Simulations of force interactions with six unequal symmetry sites on the model sample surface strongly suggest that the experimental tip

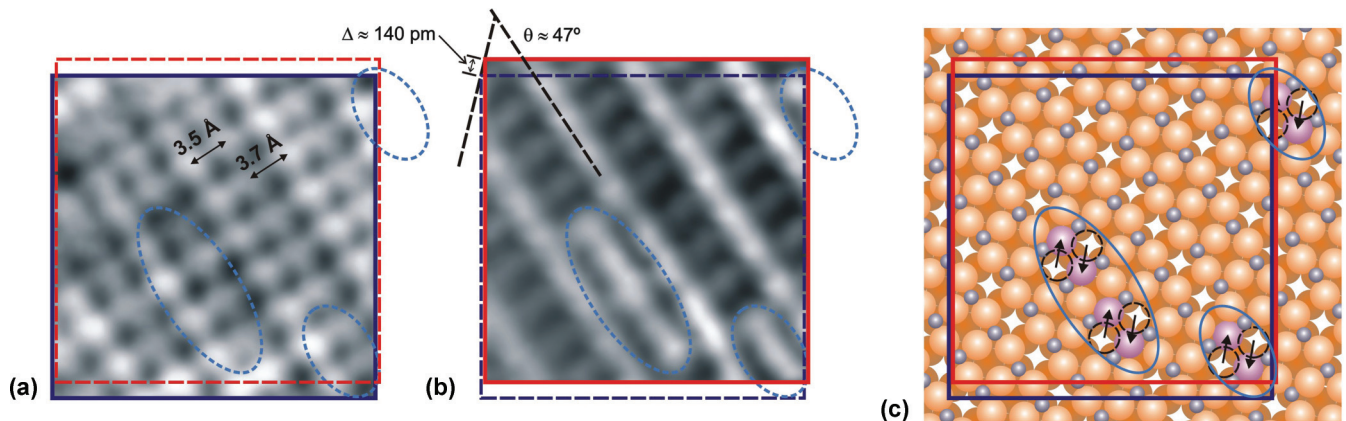


FIG. 4. (Color online) Simultaneous 3D-AFM and tunneling current measurements on Cu(100)-O (2.89×2.89 nm). (a) Horizontal force map cut from the data set shown in Fig. 3 at the distance of closest approach. Circular maxima reveal the oxygen atoms’ alternating spacing of $3.5/3.7$ Å. Total force contrast is 23 pN; dashed lines circle the locations of defects identified from the current map in Fig. 2(b). (b) Tunneling current data displaying a *ladder*-type contrast as well as defects in the form of apparent *nonmissing rows*. The gray scale covers the range of 0 – 7 pA (dark to bright). (c) Structural model of the imaged area where defects formed through lateral movement of Cu₂ atoms are highlighted. Comparing (a) and (b) reveals that the current and force images are offset by ≈ 140 pm.

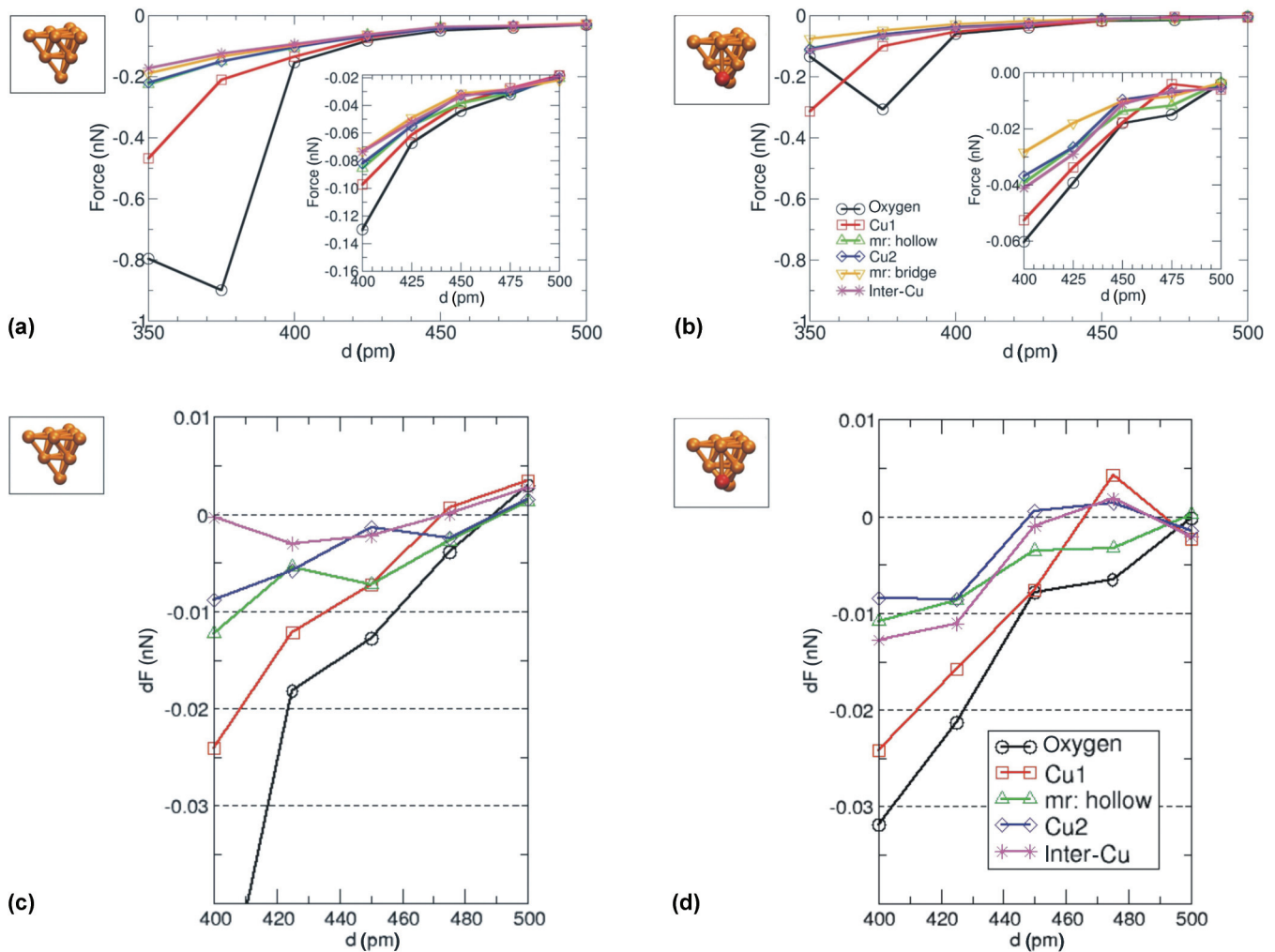


FIG. 6. (Color online) Force-distance curves computed for (a) Cu and (b) CuO tips (insets: zoom of the forces in the 400–500-pm distance range). (c) and (d) display, for Cu and CuO tips, the force difference (dF) between individual lattice sites and the missing-row bridge site (mr:bridge) located between two Cu atoms on both sides of a missing row. A comparison with experimental force contrast reveals that the closest tip-sample distance during the experiments is 425–450 pm.

has a Cu-terminated apex: Force-distance curves for the two Cu-terminated tips [(a) and (d) in Fig. 5], shown in Fig. 6, indicate that both tips interact most strongly with the O atom on the surface, although the reactivity of the O-contaminated tip is reduced. By relating the difference between computed force curves associated with individual lattice sites for the two types of tip apices [see Figs. 6(c) and 6(d)] to experimental force contrasts in the plane of closest approach, we estimated the smallest experimental tip-surface distance to be 425–450 pm where structural rearrangement of both tip and surface was negligible.

Based on this insight into the chemical and structural identities of the tip apex used in the experiments, the simultaneously recorded tunneling current can be considered [Fig. 4(b)]. Force and tunneling current channels exhibit vastly different contrasts with the current channel displaying a *ladder*-type contrast where bright rows of current maxima are interconnected by faint *bridges*. In contrast to the force channel, the assignment of maxima is more involved because two lattice sites (the Cu1 atoms as well as the fourfold coordinated hollow

sites between the Cu1 and the Cu2 atoms) feature the correct symmetry, and a possible lateral shift between the force and the current channels caused by the different physical nature of the tracked interactions^{19,57} prevents us from simply carrying the lattice assignment from the force channel over into the current channel. Nevertheless, current map simulations reveal that, for all copper-terminated tips profiling at tip-sample distances of ≈ 450 pm that we considered, the predicted contrasts match well with the experimentally observed data [see Fig. 7(e)]. Using the simulated images, we can, therefore, identify current maxima as Cu1 atoms while the faint bridges mark the positions of the electronic density shared by Cu2 atoms. Thus, combining force-based oxygen imaging with current-based Cu imaging results in chemically selective simultaneous imaging of two atomic species.

With the assignment of the maxima completed, we move to a more detailed analysis of the data. Three aspects stand out: First, defects in the form of what appear to be *nonmissing rows* are observed at several locations in the current map of Fig. 4(b). This is in stark contrast to the regular atomic

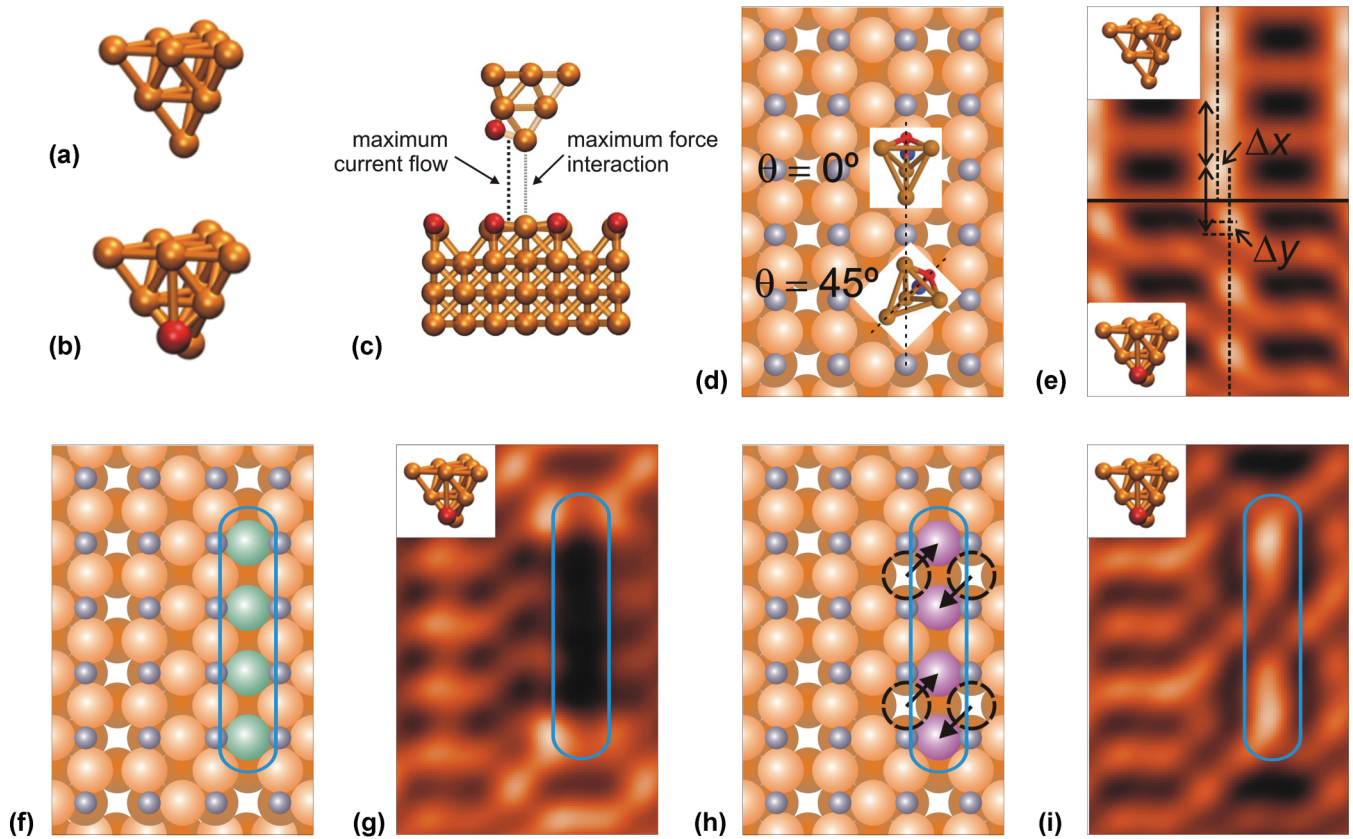


FIG. 7. (Color online) Tip and defect identification. (a) Clean Cu-terminated tip (side view). (b) Cu-terminated tip stabilized by an oxygen atom located at the side (CuO tip; side view). (c) Origin of the offset between force and current channels for the CuO tip: The oxygen atom close to the apex causes the current maximum to shift towards the direction of the oxygen, whereas, the strongest force interaction remains with the apex atom. (d) Structural model for the defect-free surface; insets of tip models define the notation used to describe tip orientation. (e) Corresponding simulated STM signature, revealing a ladder-type contrast. The upper panel has been computed for a symmetric Cu tip, and the bottom panel has been computed for a CuO tip with $\theta = 45^\circ$. The offsets resulting from tip asymmetry are highlighted. (f) and (g) Model and computed STM signatures for a missing row partially filled with four Cu atoms (filled-row defect, represented by green spheres in blue enclosure). Simulations for a CuO tip with $\theta = 45^\circ$ predict a *dark row* along the defect in strong contrast to experimental results. (h) Energetically favorable defect model created by lateral displacement of Cu2 atoms (purple spheres, highlighted by blue enclosure). For this “displacement defect,” distortions in the positions of the O atoms are minimal both in lateral and in vertical directions. (i) Corresponding STM image calculated for a CuO tip with $\theta = 45^\circ$. The appearance of an apparent *nonmissing row* is clearly observed along the length of the defect. All current maps are calculated at a constant height of 450 pm and at a bias voltage of -0.4 V.

arrangement observed in the force map and highlights the additional information that recording multiple data channels can provide. Second, despite apparent regularity, force maxima in Fig. 4(a) feature clearly visible *variations in force interaction*. Finally, the last—and more subtle—effect is the fact that the assignment of maxima results in an *offset between the force and the current channels* of (140 ± 10) pm that forms an angle of $\theta = (47 \pm 3)^\circ$ with respect to the direction of the missing rows [Fig. 4(b)]. The existence of such offsets is a well-known fact in the SPM community, but even though values in the same range have previously been reported,^{19,57} no quantitative explanation has been provided so far.

Here, we tackle this problem and show that we are able to relate the large offset with the chemical termination of the experimental tip. First, we performed tip approach simulations, which revealed that pure Cu tips [Fig. 5(a)] exhibit a degree of reactivity that makes them easily pick up O atoms on this surface, with jump-to-contact events being

observed at 375 pm. This oxygen affinity of the tip may lead to O-atom contamination close to the Cu apex [CuO tip; Fig. 5(d)], which then introduces an asymmetry into the tip that has consequences for both force and current contrasts. Adverse effects on image contrast are, however, small for forces: Systematic tip approach calculations performed on various lattice sites have shown that the location where the force maximum is observed shifts only slightly, remaining within 25-pm distance from the Cu apex atom for most tip-sample distances and tip orientations covered. But unlike the force channel, the asymmetry effect is significantly more pronounced in the STM channel as illustrated in Fig. 7(e) where a current image for a 45° rotated CuO tip (bottom part) is compared to the current image simulated for a pure copper tip (top part). In this case, the apparent offset of the current maxima from the actual locations of the Cu1 highlighted by the pure Cu tip atoms is $\Delta x = 73.6$ and $\Delta y = 66.2$ pm, which results in a total offset of roughly 100 pm in the direction of

the contaminating oxygen atom [see Fig. 7(d) for a structural model and the definition of the rotational angles]. Additional calculations performed for tip orientations of 0° , 30° , 45° , 60° , and 90° revealed that the location of maximum current always moves roughly 100 pm away from directly below the Cu apex atom towards the direction of the O atom as illustrated in Fig. 7(c). This leads us to conclude that both the Cu apex and the contaminant O atoms contribute to the tunneling current during STM image acquisition. Combined, the asymmetry effects in the SPM measurements lead to an apparent offset between force and current channels for the 45° rotated CuO tip that matches well with the experimental observation within the expected accuracy of this approach. We note that, in our analysis, we have not considered the possible influence of the local contact potential differences on the tip-sample force that has been recently discussed by Sadeghi *et al.*⁵⁸ We expect this effect to be small in our case as we are dealing with essentially metallic Cu samples with just a single monolayer of CuO oxide on top, the tip apex is contaminated with the sample material, and we are using a small bias voltage (-0.4 V).

To clarify the nature of the surface defects, the calculations were extended to consider a number of potential candidates in the form of adsorbed atoms of C, H, O, and Cu (type-I defect) as well as structural changes involving the lateral displacement of Cu atoms in an enlarged unit cell (type-II defect). Geometries for type-I adatom defects reveal that the introduction of the adatom species Cu, O, C, and H into surface and subsurface layers of the missing row area results in localized bond stretching and surface distortions with neighboring O atoms displaced up to $\Delta z = +0.4$ Å (depending on the adatom species) around the filled-row defects. Such features, illustrated in Figs. 8(a) and 8(b), are notably absent in experimental oxygen-sensitive AFM images. In addition, simulated STM images [Fig. 7(g)] predict the protruding O surface atoms to become the dominating image features, whereas, the adatoms located along the missing rows ought to appear as empty states, which conflicts with the observed experimental STM image contrast [e.g., Fig. 4(b)]. The alternative defect structure (type II) was generated by a 90° rotation of two Cu₂ atom pairs in a 4×6 Cu(100)-O unit cell. The resulting surface geometry featured negligible vertical displacement of O atoms (≈ 0.01 Å) and lateral shifts smaller than 0.05 Å. Cu atoms suffered more displacement: Cu₂ pairs in the nondefect row rise up to 0.03 Å, in particular, the pairs adjacent to the rotated Cu₂ defect. This indicates residual surface strain in the 4×6 unit cell as due to periodic boundary conditions; the nondefect rows are effectively sandwiched between defect rows and are unable to fully relax. Corresponding STM images clearly identify the displacement defects in the missing row but also exhibit brighter Cu₂ features adjacent to the Cu defect pairs that are not seen in the experiments [see Fig. 7(i)]. These features can be related to the spurious interaction between the long-range elastic strain fields induced by the defects in neighboring cells that is still present even in our rather large supercell. Computed defect formation energy of 0.23 eV for two defect pairs in a unit cell is low enough to suggest easy defect formation at room temperature.

Consequently, using energetic, geometric, and current signature considerations as described above, the defect can

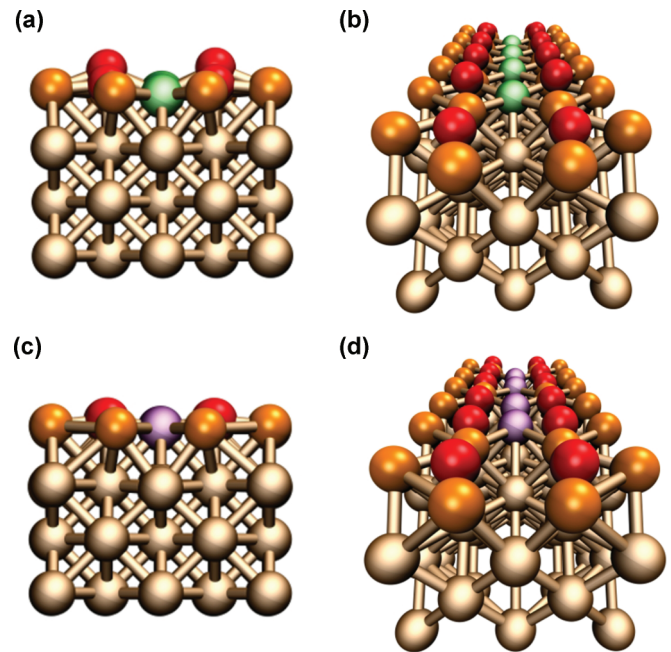


FIG. 8. (Color online) The 2×6 unit-cell segment of the optimized Cu(100)-O surface oxide structure containing defect atoms in the missing row with Cu atoms shown in gold, O atoms shown in red, and subsurface Cu slabs shown in dimmed gray. Filled-row and displacement Cu defects are colored green and purple, respectively. (a) and (c) The vertical displacement of surface atoms around the defect-filled missing row seen in the x - z plane (side view), demonstrating the additional displacement of O atoms around the filled-row defects in comparison to the case of displacement defects. (b) and (d) The difference in O- and Cu₂-atom lateral displacements towards the defect-filled missing row, perspective view.

be identified as representing a lateral displacement of Cu₂ atoms described in Figs. 4(c) and 7(h). As one can infer from the simulations, the type-II defect, produced by the model of Fig. 7(h), leads to the detection of an *apparent nonmissing row* in the current data similar to the experimental observation [Fig. 7(i)]. Such displacement defects are common in directional monolayer reconstructions as they allow them to partially equilibrate their intrinsic uniaxial stress by introducing a 90° turn of the missing row.⁵⁹ Ultimately, they may lead to the growth of perpendicular structural domains as frequently observed on Cu(100)-O.³⁵⁻⁴⁰ Due to minimal displacement of oxygen atoms (≈ 1 pm in contrast to ≈ 40 -pm vertical displacement near type-I defects), oxygen-sensitive force images do not directly reveal the presence of any of these defects. As demonstrated with these results, the capacity to uncover novel information by combining images obtained simultaneously through different contrast mechanisms, which helped to identify the surface defect in this paper, is a major advantage of multichannel imaging techniques.

Finally, we turn our attention to the atom-specific characterization of the interaction forces. Using vertical force maps, such as the one depicted as part of Fig. 3, one can study the evolution of chemical interaction forces with increasing distance from the surface. The total force corrugation in the plane of closest approach is ≈ 23 pN, which corresponds to only 1.7% of the maximum force detected within that plane

(-1.34 nN) but agrees well with the DFT prediction for the CuO tip at distances of 425–450 pm (see Fig. 6). As expected, the force corrugation decreases with increasing distance and disappears ≈ 250 pm above the plane of closest approach. In addition, substantial differences between the chemical interaction forces associated with individual O atoms of up to ≈ 9 pN (or $\approx 40\%$ of the total force contrast) are found both in the 3D map of Fig. 3 as well as in the horizontal force map of Fig. 4(a) where they manifest as uneven brightness of force maxima. Using the findings established in the previous paragraphs, the force modulation can be concluded to reflect the defect-induced inhomogeneous chemical and structural environment revealed in the tunneling current image.

V. SUMMARY

We have presented the results of a study combining the application of 3D-AFM with simultaneous recording of tunneling current and *ab initio* DFT calculations on the model sample surface of Cu(100)-O. This combined approach allowed not only the full three-dimensional characterization of atomic-scale interaction forces associated with oxygen atoms on the sample surface, but also the species-selective imaging of oxygen and copper, which ultimately allowed the detection and identification of surface defects in the form of dislocated Cu atoms. Moreover, our results show that 3D-AFM can detect

variations in local tip-surface interactions even for atoms of the same chemical species. This demonstration further underlines the versatility of high-resolution scanning probe measurement technologies: As the variations ultimately reflect changes in the local chemical environment due to, e.g., structural defects, it opens the door for studies of how the presence of a defect modifies the interactions of the affected atoms with their environment.

ACKNOWLEDGMENTS

Financial support from the US Department of Energy (Basic Energy Sciences Grant No. DE-FG02-06ER15834), the National Science Foundation through the Yale Materials Research Science and Engineering Center (Grants Nos. MRSEC DMR-1119826 and No. DMR-0520495) and the Materials World Network program (Grant No. MWN DMR-0806893), the Spanish MINECO (Projects No. MAT2008-02953-E, No. MAT2011-023627, and No. CSD2010-00024), and from the UAM-Banco Santander Program of Collaboration with the United States is gratefully acknowledged. Access to the Magerit Supercomputer (CesViMa, Madrid) was provided through the Spanish Supercomputing Network (RES, Spain). H.M. thanks the Deutsche Forschungsgemeinschaft (DFG) for support through the transregional collaborative research center TRR 061 (Project No. B7).

*These authors contributed equally to this work.

†Corresponding author: ruben.perez@uam.es

‡Corresponding author: udo.schwarz@yale.edu

¹I. Chorkendorff and J. W. Niemantsverdriet, *Concepts of Modern Catalysis and Kinetics* (Wiley-VCH, Weinheim, 2003).

²J. M. Thomas and W. J. Thomas, *Principles and Practice of Heterogeneous Catalysis* (VCH, New York, 1997).

³R. T. Vang, J. V. Lauritsen, E. Laegsgaard, and F. Besenbacher, *Chem. Soc. Rev.* **37**, 2191 (2008).

⁴E. I. Altman and U. D. Schwarz, *Adv. Mater.* **22**, 2854 (2010).

⁵R. E. Tanner, Y. Liang, and E. I. Altman, *Surf. Sci.* **506**, 251 (2002).

⁶T. Zambelli, J. Trost, J. Wintterlin, and G. Ertl, *Phys. Rev. Lett.* **76**, 795 (1996).

⁷L. Osterlund, M. O. Pedersen, I. Stensgaard, E. Laegsgaard, and F. Besenbacher, *Phys. Rev. Lett.* **83**, 4812 (1999).

⁸F. Besenbacher, *Rep. Prog. Phys.* **59**, 1737 (1996).

⁹J. Wintterlin, S. Volkening, T. V. W. Janssens, T. Zambelli, and G. Ertl, *Science* **278**, 1931 (1997).

¹⁰S. Morita, R. Wiesendanger, and E. Meyer, *Noncontact Atomic Force Microscopy* (Springer, Berlin, 2002).

¹¹M. A. Lantz, H. J. Hug, R. Hoffmann, P. J. A. Van Schendel, P. Kappenberger, S. Martin, A. Baratoff, and H.-J. Güntherodt, *Science* **291**, 2580 (2001).

¹²C. Barth, A. S. Foster, C. R. Henry, and A. L. Schluger, *Adv. Mater.* **23**, 477 (2011).

¹³Y. Sugimoto, P. Pou, M. Abe, P. Jelinek, R. Perez, S. Morita, and O. Custance, *Nature (London)* **446**, 64 (2007).

¹⁴L. Gross, F. Mohn, N. Moll, P. Liljeroth, and G. Meyer, *Science* **325**, 1110 (2009).

¹⁵L. Gross, F. Mohn, N. Moll, B. Schuler, A. Criado, E. Guitián, D. Peña, A. Gourdon, and G. Meyer, *Science* **337**, 1326 (2012).

¹⁶J. Welker and F. J. Giessibl, *Science* **336**, 444 (2012).

¹⁷F. Mohn, L. Gross, N. Moll, and G. Meyer, *Nat. Nanotechnol.* **7**, 227 (2012).

¹⁸M. Z. Baykara, T. C. Schwendemann, E. I. Altman, and U. D. Schwarz, *Adv. Mater.* **22**, 2838 (2010).

¹⁹B. J. Albers, T. C. Schwendemann, M. Z. Baykara, N. Pilet, M. Liebmann, E. I. Altman, and U. D. Schwarz, *Nat. Nanotechnol.* **4**, 307 (2009).

²⁰A. Schwarz, H. Hölscher, S. M. Langkat, and R. Wiesendanger, *AIP Conf. Proc.* **696**, 68 (2003).

²¹Y. Sugimoto, K. Ueda, M. Abe, and S. Morita, *J. Phys.: Condens. Matter* **24**, 084008 (2012).

²²E. N. Voloshina, Y. S. Dedkov, S. Torbrügge, A. Thissen, and M. Fonin, *Appl. Phys. Lett.* **100**, 241606 (2012).

²³T. König, G. H. Simon, H.-P. Rust, and M. Heyde, *Appl. Phys. Lett.* **95**, 083116 (2009).

²⁴V. E. Henrich and P. A. Cox, *The Surface Science of Metal Oxides* (Cambridge University Press, Cambridge, UK, 1996).

²⁵J. V. Lauritsen and M. Reichling, *J. Phys.: Condens. Matter* **22**, 263001 (2010).

²⁶D. A. Bonnell and J. Garra, *Rep. Prog. Phys.* **71**, 044501 (2008).

²⁷S. V. Didiulis, K. D. Butcher, S. L. Cohen, and E. I. Solomon, *J. Am. Chem. Soc.* **111**, 7110 (1989).

²⁸X. Q. Wang, J. A. Rodriguez, J. C. Hanson, D. Gamarrá, A. Martínez-Arias, and M. Fernández-García, *J. Phys. Chem. B* **110**, 428 (2006).

- ²⁹P. G. Smirniotis, D. A. Pena, and B. S. Uphade, *Angew. Chem., Int. Ed.* **40**, 2479 (2001).
- ³⁰H. H. Kan and J. F. Weaver, *Surf. Sci.* **603**, 2671 (2009).
- ³¹E. I. Altman, *Surf. Sci.* **603**, 2669 (2009).
- ³²G. Zheng and E. I. Altman, *Surf. Sci.* **504**, 253 (2002).
- ³³G. Zheng and E. I. Altman, *Surf. Sci.* **462**, 151 (2000).
- ³⁴J. Bamidele, Y. Kinoshita, R. Turanský, S. H. Lee, Y. Naitoh, Y. J. Li, Y. Sugawara, I. Štich, and L. Kantorovich, *Phys. Rev. B* **86**, 155422 (2012).
- ³⁵F. M. Leibsle, *Surf. Sci.* **337**, 51 (1995).
- ³⁶M. Kittel, M. Polcik, R. Terborg, J.-T. Hoeft, P. Baumgärtel, A. M. Bradshaw, R. L. Toomes, J.-H. Kang, D. P. Woodruff, M. Pascal, C. L. A. Lamont, and E. Rotenberg, *Surf. Sci.* **470**, 311 (2001).
- ³⁷M. J. Harrison, D. P. Woodruff, J. Robinson, D. Sander, W. Pan, and J. Kirschner, *Phys. Rev. B* **74**, 165402 (2006).
- ³⁸M. Lampimäki, K. Lahtonen, M. Hirsimäki, and M. Valden, *J. Chem. Phys.* **126**, 034703 (2007).
- ³⁹K. Tanaka, T. Fujita, and Y. Okawa, *Surf. Sci.* **401**, L407 (1998).
- ⁴⁰C. Wöll, R. J. Wilson, S. Chiang, H. C. Zeng, and K. A. R. Mitchell, *Phys. Rev. B* **42**, 11926 (1990).
- ⁴¹B. J. Albers, M. Liebmann, T. C. Schwendemann, M. Z. Baykara, M. Heyde, M. Salmeron, E. I. Altman, and U. D. Schwarz, *Rev. Sci. Instrum.* **79**, 033704 (2008).
- ⁴²F. J. Giessibl, *Appl. Phys. Lett.* **76**, 1470 (2000).
- ⁴³B. J. Albers, T. C. Schwendemann, M. Z. Baykara, N. Pilet, M. Liebmann, E. I. Altman, and U. D. Schwarz, *Nanotechnology* **20**, 264002 (2009).
- ⁴⁴M. Z. Baykara, O. E. Dagdeviren, T. C. Schwendemann, H. Mönig, E. I. Altman, and U. D. Schwarz, *Beilstein J. Nanotechnol.* **3**, 637 (2012).
- ⁴⁵G. Kresse and J. Furthmüller, *Phys. Rev. B* **54**, 11169 (1996).
- ⁴⁶P. E. Blochl, *Phys. Rev. B* **50**, 17953 (1994).
- ⁴⁷G. Kresse and D. Joubert, *Phys. Rev. B* **59**, 1758 (1999).
- ⁴⁸J. P. Perdew, K. Burke, and M. Ernzerhof, *Phys. Rev. Lett.* **77**, 3865 (1996).
- ⁴⁹N. Bonini, A. Kokalj, A. Dal Corso, S. de Gironcoli, and S. Baroni, *Surf. Sci.* **600**, 5074 (2006).
- ⁵⁰H. C. Zeng, R. A. McFarlane, and K. A. R. Mitchell, *Surf. Sci.* **208**, L7 (1989).
- ⁵¹T. Ozaki and H. Kino, *Phys. Rev. B* **69**, 195113 (2004).
- ⁵²I. Morrison, D. M. Bylander, and L. Kleinman, *Phys. Rev. B* **47**, 6728 (1993).
- ⁵³J. M. Blanco, F. Flores, and R. Perez, *Prog. Surf. Sci.* **81**, 403 (2006).
- ⁵⁴G. H. Enevoldsen, H. P. Pinto, A. S. Foster, M. C. R. Jensen, A. Kühnle, M. Reichling, W. A. Hofer, J. V. Lauritsen, and F. Besenbacher, *Phys. Rev. B* **78**, 045416 (2008).
- ⁵⁵A. Schwarz, W. Allers, U. D. Schwarz, and R. Wiesendanger, *Phys. Rev. B* **61**, 2837 (2000).
- ⁵⁶P. Pou, S. A. Ghasemi, P. Jelinek, T. Lenosky, S. Goedecker, and R. Perez, *Nanotechnology* **20**, 264015 (2009).
- ⁵⁷S. Hembacher, F. J. Giessibl, J. Mannhart, and C. F. Quate, *Proc. Natl. Acad. Sci. USA* **100**, 12539 (2003).
- ⁵⁸A. Sadeghi, A. Baratoff, S. A. Ghasemi, S. Goedecker, T. Glatzel, S. Kawai, and E. Meyer, *Phys. Rev. B* **86**, 075407 (2003).
- ⁵⁹M. Li, E. I. Altman, A. Posadas, and C. H. Ahn, *J. Vac. Sci. Technol. A* **22**, 1682 (2004).